Continuum Mech. Thermodyn. (2022) 34:165–184
https://doi.org/10.1007/s00161-021-01052-w

ORIGINAL ARTICLE

Thomas Obermayer · **Christian Krempaszky** · **Ewald Werner**

Determination of the anisotropic elasticity tensor by mechanical spectroscopy

Received: 18 March 2021 / Accepted: 8 September 2021 / Published online: 11 October 2021

Abstract A method is proposed to identify the fully anisotropic elasticity tensor by applying the impulse excitation technique. A specially designed batch of several differently oriented bar-shaped specimens with rectangular cross section is analyzed with respect to the eigenfrequencies of their fundamental flexural and torsional modes. Estimations based on the equations for the calculation of the isotropic Young's modulus and the shear modulus from the ASTM standard allow a first approximation of the elasticity tensor from a selected subset of the measured eigenfrequencies. Subsequently, a more precise determination of the elasticity tensor is achieved by a numerical modal analysis using the finite element method. In this course, a Newton–Raphson optimization method is applied to solve the inverse problem. The proposed approach is demonstrated on a batch of specimen fabricated from the nickel-base alloy IN718 by selective laser melting.

Keywords Mechanical spectroscopy · Inverse problem · Impulse excitation technique · Anisotropic elasticity · Additive manufacturing

1 Introduction

The determination of isotropic elastic properties by the impulse excitation technique (IET) is well established and standardized [1]. A specimen is excited by the impact of a needle-shaped projectile to vibration, allowing to calculate the dynamic moduli from the eigenfrequencies obtained in the recorded sound spectrum [2]. Dynamic methods for the characterization of elastic behavior, such as IET, show several advantages compared to static methods: The results are highly accurate, a wide range of specimen geometries is suitable and the experimental setup is inexpensive and easy to handle [3,4]. Furthermore, the measured frequency spectrum contains more information with regard to the elastic response than the stress–strain relation obtained by static methods, which is particularly useful in connection with anisotropic behavior. Isotropic elastic constants can directly be calculated by equations in closed form from the fundamental eigenfrequencies, whereby in case of anisotropy the elastic constants have to be determined by solving an inverse problem involving several eigenfrequencies. For orthotropic plates with known orientation of planes of material symmetry, the in-plane engineering constants can be evaluated following the Resonalyzer method [5]. This approach is particularly relevant for fiber-reinforced composite plates and metal sheets, because in these cases the orientations of planes of material symmetry are known by their relation to the direction of the reinforcement or to the rolling direction [6–8]. IET was also successfully applied for the determination of the elastic constants of single crystals and their orientation from the eigenfrequencies of specimens, consisting of equally oriented crystals [9]. Further

Communicated by Andreas Öchsner.

T. Obermayer (✉) · C. Krempaszky · E. Werner
Institute of Materials Science and Mechanics of Materials, Technical University of Munich, Boltzmannstraße 15, 85748 Garching, Germany
E-mail: obermayer@wkm.mw.tum.de

methods exist for the characterization of the elastic behavior of directionally solidified alloys or directionally recrystallized alloys, where the texture is known [10].

In case of additively manufactured alloys, the texture and consequently the anisotropic elastic behavior strongly depend on various process parameters and on the scanning strategy. These dependencies are subject of current research, giving rise to a greater need for direct determination of the fully anisotropic elasticity tensor without any a priori knowledge of the class of material symmetry or the orientation of possible planes of material symmetry besides methods based on texture measurements and ultrasound spectroscopy [11, 12]. Within the scope of this contribution, a method is presented to determine all 21 components of the elasticity tensor by IET, in order to capture the complete elastic behavior resulting from any potentially complex texture, caused by the manufacturing process. Initial considerations of this approach were proposed by the authors in [13]. In this course, a specially designed batch of several differently oriented specimens with rectangular cross section is analyzed with respect to the eigenfrequencies of their fundamental flexural and torsional eigenmode. Estimations based on the equations in closed form for the calculation of the isotropic Young's modulus and the shear modulus from the ASTM standard allow to formulate the method under consideration of stability with respect to measurement deviations and additionally enable a first approximation of the elasticity tensor from a selected subset of the experimentally determined eigenfrequencies. Subsequently, the Newton–Raphson optimization method in combination with a numerical modal analysis using the finite element method (FEM) is applied to identify the components of the elasticity tensor that fit the experimentally determined eigenfrequencies best. The proposed approach is demonstrated on a batch of specimens fabricated from the nickel-base alloy IN718 by selective laser melting (SLM). A comparison between the experimentally determined eigenfrequencies, that do not contribute to the optimization scheme, and the ones predicted on the basis of the determined elasticity tensor allows to verify the result. An analysis of the harmonic decomposition of the elasticity tensor as well as the corresponding dilatational modulus and the Voigt tensor indicates the validity of the results.

2 Estimation of elastic constants by IET

The resonant frequencies of a solid depend on the geometry, the density, the elastic properties and the damping of the material. Neglecting the material damping results in the equality of resonant frequencies and corresponding undamped eigenfrequencies. In case of linear elasticity, the elastic properties are specified by the elasticity tensor C_{ijkl}, or by the compliance tensor S_{ijkl}, which relate the stress tensor σ_{ij} and the strain tensor ε_{ij} by Hooke's law in its general form:

$$\sigma_{ij} = C_{ijkl}\,\varepsilon_{kl}, \tag{1}$$

$$\varepsilon_{ij} = S_{ijkl}\,\sigma_{kl}. \tag{2}$$

Due to the minor symmetries, $S_{ijkl} = S_{jikl} = S_{ijlk} = S_{jilk}$, and the major symmetry, $S_{ijkl} = S_{klij}$ of the compliance tensor, 21 of its 81 components describe the complete elastic behavior in the most general anisotropic case.

In the special case of isotropy, all components can be specified by two independent elastic constants, e.g., by Young's modulus E and shear modulus G:

$$S_{ijkl} = \left(\frac{1}{E} - \frac{1}{2\,G}\right)\delta_{ij}\,\delta_{kl} + \frac{1}{4\,G}\left(\delta_{ik}\,\delta_{jl} + \delta_{il}\,\delta_{jk}\right), \tag{3}$$

where δ_{ij} denotes the Kronecker delta. The determination of these constants from the fundamental eigenfrequencies of a specimen is standardized by the ASTM and is discussed in Sect. 2.1. However, in case of full anisotropy all 21 components are to be determined. This leads to an inverse problem, which is covered by the proposed method.

In order to provide a closed-form estimation of the elastic constants even in the anisotropic case, a modification of these relations is proposed in this section.

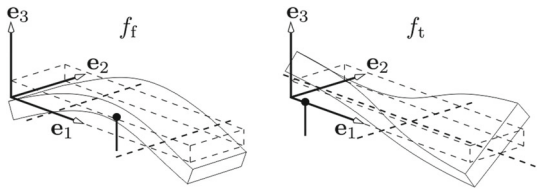

Fig. 1 Sketch of the experimental setup, showing the specimen supported by wires in the vibration nodes and the impact point of the projectile for the excitation of the fundamental flexural eigenfrequency f_f and the fundamental torsional eigenfrequency f_t

2.1 Determination of isotropic elastic constants

Depending on the elastic modulus to be examined, the specimen geometry must be chosen properly. The ASTM standard for measurement of isotropic elastic properties suggests cylindrical specimens as well as bars with rectangular cross section [1]. Cylindrical specimens are suited for the determination of the Young's modulus from the fundamental flexural eigenfrequency f_f, whereas bars with rectangular cross section allow additionally to identify the shear modulus from the fundamental torsional eigenfrequency f_t. In order to allow an almost free vibration, the specimen is supported in the vibration nodes of the eigenmode corresponding to the eigenfrequency to be measured, while the impact point of the excitation projectile is selected such that the eigenfrequency is sufficiently excited, as shown in Fig. 1.

In case of isotropic elasticity the Young's modulus E can be calculated based on Euler–Bernoulli's beam theory according to:

$$E = \frac{0.9465\, T_1\, m\, l^3\, f_\mathrm{f}^2}{b\, t^3}. \tag{4}$$

The correction factor T_1 depends mainly on the ratio of thickness t to length l and is close to one in case of slender specimen geometries, as it accounts for the influence of transverse shear deformation in the corresponding eigenmode. For the calculation of the shear modulus G, the following empirical equation applies:

$$G = \frac{4\, B\, m\, l\, f_\mathrm{t}^2}{(1 + A)\, b\, t}. \tag{5}$$

The constants A and B strongly depend on the ratio of thickness t to width b and hence essentially contribute to the calculation of the shear modulus. The influence of the density is implicitly considered by the mass m of the specimen.

2.2 Estimation of components of the compliance tensor for anisotropic elasticity

In case of fully anisotropic elastic behavior, the eigenfrequencies depend on several elastic constants, whereby these relations are not known in closed form. Leissa [14] suggests an approximation for the eigenfrequencies of plates in case of orthotropic anisotropy in closed form. However, these equations only apply, if the planes of material symmetry are parallel to the edges of the plate. In the most general case of arbitrary planes of material symmetry the eigenfrequencies can be calculated by a numerical modal analysis using FEM, but, in contrast to the isotropic case, the corresponding inverse problem cannot be solved in closed form. Nevertheless, to estimate certain components of the compliance tensor with respect to the specimen basis ($\mathbf{e}_1, \mathbf{e}_2, \mathbf{e}_3$), which is shown in Fig. 1, we propose to modify the standardized relationships for isotropic elasticity.

In the fundamental flexural eigenmode, the normal strain in the longitudinal direction of the specimen is predominant. Consequently, the Young's modulus E in Eq. (4) is replaced by the Young's modulus E_1 in the longitudinal direction of the specimen, which is the reciprocal of the component S_{1111} of the compliance tensor with respect to the specimen basis:

$$S_{1111} = \frac{1}{E_1} = \frac{b\, t^3}{0.9465\, T_1\, m\, l^3\, f_\mathrm{f}^2}. \tag{6}$$

In case of slender specimens, the fundamental torsional eigenfrequency is significantly influenced by the shear modulus G_{12}, due to the predominant shear deformation in the specimen plane occurring in the corresponding

fundamental eigenmode. The reciprocal of the shear modulus G_{12} is directly related to the component S_{1212} of the compliance tensor. This relation allows to estimate S_{1212} by substituting the shear modulus G by the shear modulus G_{12} in the specimen plane, by modification of Eq. (5):

$$S_{1212} = \frac{1}{4\,G_{12}} = \frac{(1+A)\;b\,t}{16\,B\,m\,l\,f_{\mathrm{t}}^2}. \tag{7}$$

The relations (6) and (7) show that the estimations are highly sensitive with respect to the specimen thickness. Hence, in order to enable an accurate determination of the elastic constants from the measured eigenfrequencies, it is essential to manufacture specimens with high precision in parallelism of the specimen sides and to measure the specimen dimensions at high accuracy.

Theoretically, also higher-order flexural eigenfrequencies, higher-order torsional eigenfrequencies, as well as the eigenfrequencies of longitudinal vibration modes could be taken into account. However, under the assumption of homogeneous elastic behavior, higher-order eigenfrequencies contain almost the same information concerning the elastic properties as the fundamental ones. The eigenfrequencies of longitudinal modes depend mostly on the Young's modulus E_1, similar to the flexural eigenfrequencies. Furthermore, the longitudinal eigenmodes are difficult to excite using the impulse excitation setup, see Fig. 1. In addition, it is difficult to realize a free vibration corresponding to higher-order eigenmodes, due to the required highly precise support of the specimen in the vibration nodes. Therefore, only the fundamental flexural frequency and the fundamental torsional frequency are considered in the proposed method, as specified by the ASTM standard in case of isotropic elastic behavior.

2.3 Verification of the estimations of the compliances

The proposed estimations of S_{1111} and S_{1212} are verified by comparing the fundamental eigenfrequencies calculated by rearranging Eqs. (6) and (7), which are referred to as $f_{\mathrm{f}}^{\mathrm{Est}}$ and $f_{\mathrm{t}}^{\mathrm{Est}}$ with the corresponding ones calculated by numerical modal analysis using FEM, which are denoted by $f_{\mathrm{f}}^{\mathrm{FEM}}$ and $f_{\mathrm{t}}^{\mathrm{FEM}}$. This calculation of the eigenfrequencies from the elastic constants represents the direct problem of the aforementioned inverse problem. Additionally, the sensitivities with respect to the components of the compliance tensor allow an explanation of the deviation between both approaches, as the finite element model takes into account all components of the compliance tensor. The deviations between the results calculated by both approaches depend significantly on the degree of anisotropy and the orientation of planes of material symmetry relative to the specimen sides. These aspects are exemplarily shown in a study by means of three different material models.

Model (a) represents isotropic elastic behavior ($E = 200$ GPa, $\nu = 0.3$), whereas in models (b) and (c) the elastic behavior of a cubic single crystal is assumed. This limiting case represents the strongest anisotropy that can result from a texture generated in the manufacturing process. The elastic constants of the IN718 single-crystal material assumed in this study are provided by Martin et al. [21] and listed in Table 8 of Sect. 4.3. The density is set to $\rho = 8.15\,\mathrm{g\,cm^{-3}}$, which is in good agreement with the experimentally obtained values, see Table 9.

Models (b) and (c) differ in the orientation of the lattice vectors, as shown in Fig. 2. In material model (b), the lattice vectors of the unit cell coincide with the specimen basis. Hence, the planes of material symmetry are parallel to the specimen sides. In contrast to that, the lattice vectors in model (c) are rotated relative to the basis vectors of the specimen coordinate system by the Euler angles with Bunge convention ($\phi_1 = -26°$, $\phi = 45°$, $\phi_2 = 0°$).

The specimen dimensions assumed in this study are identical to the ones in the experiment ($l = 65$ mm, $b = 18$ mm, $t = 4.5$ mm). The sensitivities of the estimations are calculated by rearranging Eqs. (6) and (7) and differentiation with respect to the components of the compliance tensor:

$$\frac{\partial f_{\mathrm{f}}^{\mathrm{Est}}}{\partial S_{1111}} = -\frac{1}{2}\sqrt{\frac{b\,t^3}{0.9465\,T_1\,m\,l^3}}\;(S_{1111})^{-\frac{3}{2}}, \tag{8}$$

$$\frac{\partial f_{\mathrm{t}}^{\mathrm{Est}}}{\partial S_{1212}} = -\frac{1}{8}\sqrt{\frac{(1+A)\;b\,t}{B\,m\,l}}\;(S_{1212})^{-\frac{3}{2}}. \tag{9}$$

The partial derivatives of the eigenfrequencies with respect to the compliances calculated by the numerical modal analysis are approximated by evaluation of the forward difference quotient:

$$\frac{\partial f^{\mathrm{FEM}}}{\partial S_{mnop}} = \frac{f^{\mathrm{FEM}}\left(S_{ijkl} + \delta_{im}\,\delta_{jn}\,\delta_{ko}\,\delta_{lp}\,\Delta S\right) - f^{\mathrm{FEM}}\left(S_{ijkl}\right)}{\Delta S}. \tag{10}$$

The results are listed in Table 1, showing that the estimation of the eigenfrequencies f_{f} and f_{t} for material models (a) and (b) are close to the numerically calculated results. In material model (c), larger deviations are observed.

These deviations can be discussed by the sensitivities of the eigenfrequencies with respect to the components of the compliance tensor showing the strongest impacts as outlined in Fig. 3.

The eigenfrequency f_{f} is most sensitive with respect to S_{1111}, whereby f_{t} is mainly influenced by S_{1212} as expected, but it can be seen that both eigenfrequencies are also influenced by S_{1112} and additionally f_{t} is sensitive to S_{1313}. The influence of S_{1112} becomes particularly visible in material model (c), where the lattice vectors of the unit cell are rotated, such that the absolute value of S_{1112} is maximized. Despite this influence, the estimations are acceptable, since the absolute value of S_{1112} is several times smaller than those of S_{1111} or S_{1212} at its maximum for the analyzed single-crystal material.

The sensitivity of f_{t} with respect to S_{1313} contributes particularly to the deviation of the eigenfrequency f_{t}, if the difference between S_{1212} and S_{1313} is significant. If these components are equal, as in material models (a) and (b), this shortcoming has less impact because in the estimation of f_{t}, which is based on isotropic elasticity, the influence of transverse shear deformation is considered and in case of isotropy S_{1212} and S_{1313} are equal. The influence of S_{1313} increases significantly for specimens with higher thickness to width ratio. Hence, in our work the specimen dimensions are chosen, such that the influence of S_{1313} is moderate, in order to achieve an adequate estimation of S_{1212} from f_{t} by Eq. (7), even if the difference of S_{1212} and S_{1313} is significant. The estimation of the eigenfrequencies for material model (b) are better in contrast to model (c), because in the former case $S_{1112} = 0$ and $S_{1212} = S_{1313}$.

In conclusion, the sensitivity analysis shows a nonlinear relationship between the eigenfrequencies and the components of the compliance tensor, but it can be seen that Eqs. (6) and (7) provide good estimations for the relation between the compliances and the fundamental eigenfrequencies, even for the pronounced anisotropy in case of single-crystal elastic behavior and the adverse orientation of the planes of material symmetry.

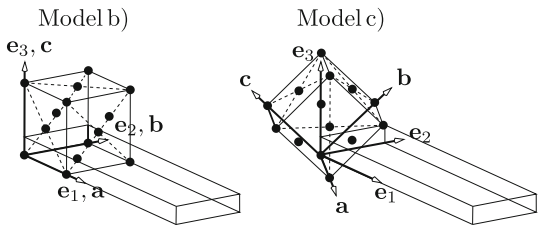

Fig. 2 Orientation of the lattice vectors (**a, b, c**) of the face centered cubic lattice relative to the specimen basis for material models (b) and (c)

Table 1 Comparison of the estimated (Est) and numerically calculated (FEM) eigenfrequencies f_{f} and f_{t} and their sensitivities for the material models (a), (b) and (c)

Model	f_{f} (Hz)	$\frac{\partial f_{\mathrm{f}}}{\partial S_{1111}}$ (10^{13} Hz Pa)	f_{t} (Hz)	$\frac{\partial f_{\mathrm{t}}}{\partial S_{1212}}$ (10^{13} Hz Pa)
(a)				
Est	5339.9	− 53.4	10575.7	− 162.7
FEM	5345.0	− 51.7	10613.0	− 138.6
(b)				
Est	4022.6	− 22.8	12623.7	− 276.7
FEM	4068.6	− 23.0	12591.0	− 234.0
(c)				
Est	4783.6	− 38.4	9406.9	− 114.5
FEM	4718.2	− 34.3	10669.0	− 134.4

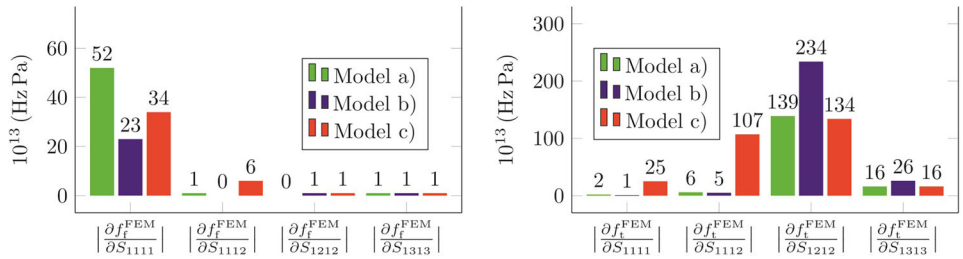

Fig. 3 Sensitivities of eigenfrequencies f_f and f_t with respect to the components of the compliance tensor showing the strongest impacts, calculated numerically

3 Determination of the elasticity tensor by solving an inverse problem

If the orientation of possible planes of material symmetry is unknown, the anisotropic elasticity tensor and hence the compliance tensor are specified by 21 independent components. For their determination from 21 eigenfrequencies of differently oriented specimens, 21 independent relations are required. These relations are not known in closed form (as discussed in Sect. 2.2), and each eigenfrequency depends on several components of the compliance tensor. Hence, the corresponding inverse problem will be solved by minimization of the deviation between the eigenfrequencies calculated numerically on the basis of the elasticity tensor to be determined and the corresponding measured ones, using the Newton–Raphson method. For this purpose, a first approximation of the compliance tensor, based on the estimations in closed form is proposed in Sect. 3.1. It allows to select the specimen orientations as well as the 21 eigenfrequencies in order to enable a robust determination of the compliance tensor as described in Sect. 3.2. Even though the convergence rate of the optimization is also high from remote starting points, it is recommended to start the optimization scheme from the approximated compliance tensor, in order to reduce the number of required iteration steps.

3.1 First approximation of the compliance tensor

The direct relations in closed form between the fundamental eigenfrequencies and certain components of the compliance tensor with respect to the specimen basis, as described in Sect. 2.2, allow to estimate compliances in arbitrary directions and/or planes by proper choice of the specimen orientation. These compliances are linearly related to the components of the compliance tensor with respect to a reference basis $\left(\mathbf{e}_{\bar{1}}, \mathbf{e}_{\bar{2}}, \mathbf{e}_{\bar{3}}\right)$, according to the transformation rule of the fourth-order compliance tensor:

$$S^{(p)}_{i\,j\,k\,l} = S_{\bar{m}\,\bar{n}\,\bar{o}\,\bar{p}}\; Q^{(p)}_{i\,\bar{m}}\, Q^{(p)}_{j\,\bar{n}}\, Q^{(p)}_{k\,\bar{o}}\, Q^{(p)}_{l\,\bar{p}}, \tag{11}$$

where $Q^{(p)}_{i\,\bar{m}}$ represent the transformation coefficients and the overlined indices refer to the reference basis, whereas the other indices refer to the basis of the corresponding specimen p. This orthogonal transformation is specified by the Tait–Bryan angles, which are addressed in Sect. 3.2. Due to the minor and major symmetries of the compliance tensor, as discussed in Sect. 2, the 81 summands can be reduced to a set of 21 independent components multiplied with corresponding adapted transformation coefficients $a^{(p)}_{\alpha\,\bar{\beta}}$, as shown in "Appendix A." This simplification allows the representation of the transformation by the independent 21 components S_α with single index and the corresponding adapted transformation coefficients $a^{(p)}_{\alpha\,\bar{\beta}}$ with double indices:

$$S^{(p)}_{\alpha} = a^{(p)}_{\alpha\,\bar{\beta}}\, S_{\bar{\beta}}, \quad \alpha, \bar{\beta} = 1 \ldots 21. \tag{12}$$

The coordinates of the compliance tensor are arranged in a symmetric matrix of dimension 6x6 by application of the common conversion of indices $ij \rightarrow I$: (11 $\rightarrow$ 1, 22 $\rightarrow$ 2, 33 $\rightarrow$ 3, 23 $\rightarrow$ 4, 13 $\rightarrow$ 5, 12 $\rightarrow$ 6),

allowing to clarify the assignment between the components in notation S_α and S_{ijkl}:[1]

$$\left[S_{\bar{I}\,\bar{J}}\right] = \left[\begin{array}{ccc|ccc} S_{\bar{1}} & S_{\bar{2}} & S_{\bar{3}} & S_{\bar{4}} & S_{\bar{5}} & S_{\bar{6}} \\ & S_{\bar{7}} & S_{\bar{8}} & S_{\bar{9}} & S_{\bar{10}} & S_{\bar{11}} \\ & & S_{\bar{12}} & S_{\bar{13}} & S_{\bar{14}} & S_{\bar{15}} \\ \hline & \text{sym} & & S_{\bar{16}} & S_{\bar{17}} & S_{\bar{18}} \\ & & & & S_{\bar{19}} & S_{\bar{20}} \\ & & & & & S_{\bar{21}} \end{array}\right] = \left[\begin{array}{ccc|ccc} S_{\bar{1}\bar{1}\bar{1}\bar{1}} & S_{\bar{1}\bar{1}\bar{2}\bar{2}} & S_{\bar{1}\bar{1}\bar{3}\bar{3}} & S_{\bar{1}\bar{1}\bar{1}\bar{3}} & S_{\bar{1}\bar{1}\bar{2}\bar{3}} & S_{\bar{1}\bar{1}\bar{1}\bar{2}} \\ & S_{\bar{2}\bar{2}\bar{2}\bar{2}} & S_{\bar{2}\bar{2}\bar{3}\bar{3}} & S_{\bar{2}\bar{2}\bar{1}\bar{3}} & S_{\bar{2}\bar{2}\bar{2}\bar{3}} & S_{\bar{2}\bar{2}\bar{1}\bar{2}} \\ & & S_{\bar{3}\bar{3}\bar{3}\bar{3}} & S_{\bar{3}\bar{3}\bar{2}\bar{3}} & S_{\bar{3}\bar{3}\bar{1}\bar{3}} & S_{\bar{3}\bar{3}\bar{1}\bar{2}} \\ \hline & \text{sym} & & S_{\bar{2}\bar{3}\bar{2}\bar{3}} & S_{\bar{2}\bar{3}\bar{1}\bar{3}} & S_{\bar{2}\bar{3}\bar{1}\bar{2}} \\ & & & & S_{\bar{1}\bar{3}\bar{1}\bar{3}} & S_{\bar{1}\bar{3}\bar{1}\bar{2}} \\ & & & & & S_{\bar{1}\bar{2}\bar{1}\bar{2}} \end{array}\right]. \tag{13}$$

In order to distinguish between the contributions of different specimens, the specimen number p is indicated by a superscript index. The component $S_1^{(p)}$ is estimated from the eigenfrequency $f_{\mathrm{f}}^{(p)}$ by Eq. (6), whereas the component $S_{21}^{(p)}$ is estimated from the eigenfrequency $f_{\mathrm{t}}^{(p)}$ by Eq. (7). Therefore, the components of the compliance tensor with respect to the reference basis are directly related to the eigenfrequencies of the specimen by the sets of adapted transformation coefficients $a_{1\,\bar{\beta}}^{(p)}$ and $a_{21\,\bar{\beta}}^{(p)}$:

$$S_1^{(p)} = a_{1\,\bar{\beta}}^{(p)}\, S_{\bar{\beta}}, \tag{14}$$

$$S_{21}^{(p)} = a_{21\,\bar{\beta}}^{(p)}\, S_{\bar{\beta}}. \tag{15}$$

These transformations can be interpreted as a scalar product of two vectors, where $\left[a_{1\,\bar{\beta}}^{(p)}\right]$ or $\left[a_{21\,\bar{\beta}}^{(p)}\right]$ denote column vectors containing the adapted transformation coefficients and $\left[S_{\bar{\beta}}\right]$ denotes a column vector containing the components of the compliance tensor with respect to the reference basis:

$$S_1^{(p)} = \left[a_{1\,\bar{\beta}}^{(p)}\right]^{\mathrm{T}} \cdot \left[S_{\bar{\beta}}\right], \tag{16}$$

$$S_{21}^{(p)} = \left[a_{21\,\bar{\beta}}^{(p)}\right]^{\mathrm{T}} \cdot \left[S_{\bar{\beta}}\right]. \tag{17}$$

Equations of type Eqs. (16) and (17) can be combined to a system of linear equations:

$$\left[M_{i\,\bar{\beta}}\right] \cdot \left[S_{\bar{\beta}}\right] = \left[b_i\right], \tag{18}$$

where the vectors containing the transformation coefficients are assembled to the matrix:

$$\left[M_{i\,\bar{\beta}}\right] = \left[\left[a_{1\,\bar{\beta}}^{(1)}\right]^{\mathrm{T}} \left[a_{21\,\bar{\beta}}^{(1)}\right]^{\mathrm{T}} \left[a_{1\,\bar{\beta}}^{(2)}\right]^{\mathrm{T}} \,..\, \left[a_{21\,\bar{\beta}}^{(k)}\right]^{\mathrm{T}}\right]^{\mathrm{T}}. \tag{19}$$

The compliances with respect to the reference basis are arranged consistently with the transformation coefficients in the column vector:

$$\left[b_i\right] = \left[S_1^{(1)}\ S_{21}^{(1)}\ S_1^{(2)}\ ..\ S_{21}^{(k)}\right]^{\mathrm{T}}. \tag{20}$$

If the resulting linear system of equations consists of 21 independent equations, it can be solved and hence provides a first approximation of the compliance tensor.

[1] This matrix representation of independent components of the compliance tensor does not correspond to an orthonormal basis.

3.2 Selection of specimen orientations

The system of linear equations for the first approximation of the compliance tensor can be solved uniquely, if the matrix $\left[M_{i\,\bar{\beta}}\right]$ has full rank. This depends on which equations of type Eqs. (16) and (17) are included in the system of equations and on the orientation of the corresponding specimens. In order to formulate the inverse problem under consideration of stability, it is of major importance that the choice of specimen orientations and the selection of equations are conceived with the objectives that measurement deviations and shortcomings of the estimations, as described in Sect. 2.1, affect the result of the first approximation as little as possible. This aspect can be evaluated by the condition number κ_2 of the matrix $\left[M_{i\,\bar{\beta}}\right]$, which specifies an upper limit of the relative error in the result caused by a relative error in the input data:

$$\frac{\left|\left|\left[\Delta S_{\bar{\beta}}\right]\right|\right|}{\left|\left|\left[S_{\bar{\beta}}\right]\right|\right|} \leq \kappa_2 \frac{\left|\left|\left[\Delta b_i\right]\right|\right|}{\left|\left|\left[b_i\right]\right|\right|}, \tag{21}$$

where $||\cdot||$ denotes the L_2-norm. The condition number is calculated by the ratio of the maximum and the minimum singular value of the matrix $\left[M_{i\,\bar{\beta}}\right]$:

$$\kappa_2 = \frac{\sigma_{\max}\left(\left[M_{i\,\bar{\beta}}\right]\right)}{\sigma_{\min}\left(\left[M_{i\,\bar{\beta}}\right]\right)}. \tag{22}$$

In order to minimize κ_2 the orientations of the specimens are selected such that a preferably low number of matrix row operations of $\left[M_{i\,\bar{\beta}}\right]$ is necessary for solving the system of linear equations. Consistent to the notation of the compliances in Eq. (13) the transformation coefficients are arranged in a matrix of same dimension in order to clarify the assignment between the coordinates of the compliance tensor and the corresponding adapted transformation coefficients. The index related to the specimen basis α is either 1 for the component $S_1^{(p)}$ or 21 for the component $S_{21}^{(p)}$:

$$\left[a^{(p)}_{\langle\alpha\rangle\,\bar{I}\,\bar{J}}\right] = \begin{bmatrix} a^{(p)}_{\alpha\,\bar{1}} & a^{(p)}_{\alpha\,\bar{2}} & a^{(p)}_{\alpha\,\bar{3}} & a^{(p)}_{\alpha\,\bar{4}} & a^{(p)}_{\alpha\,\bar{5}} & a^{(p)}_{\alpha\,\bar{6}} \\ & a^{(p)}_{\alpha\,\bar{7}} & a^{(p)}_{\alpha\,\bar{8}} & a^{(p)}_{\alpha\,\bar{9}} & a^{(p)}_{\alpha\,\bar{10}} & a^{(p)}_{\alpha\,\bar{11}} \\ & & a^{(p)}_{\alpha\,\bar{12}} & a^{(p)}_{\alpha\,\bar{13}} & a^{(p)}_{\alpha\,\bar{14}} & a^{(p)}_{\alpha\,\bar{15}} \\ & & & a^{(p)}_{\alpha\,\bar{16}} & a^{(p)}_{\alpha\,\bar{17}} & a^{(p)}_{\alpha\,\bar{18}} \\ & \text{sym} & & & a^{(p)}_{\alpha\,\bar{19}} & a^{(p)}_{\alpha\,\bar{20}} \\ & & & & & a^{(p)}_{\alpha\,\bar{21}} \end{bmatrix}. \tag{23}$$

Manufacturing of the batch of specimens via selective laser melting is done in a single job, therefore the construction volume of the 3-D printer must be efficiently used. Additionally, the specimens are post-processed after manufacturing from cylinders in order to achieve the required geometric accuracy and to avoid disturbances of the microstructure due to surface effects. The specimen orientations are specified by Tait–Bryan angles, of rotation sequence $(\mathbf{e}_{\bar{3}}, \mathbf{e}_{\bar{2}'}, \mathbf{e}_{\bar{1}''})$ with corresponding angles (ψ, θ, φ), that describe the intrinsic rotation from the reference basis to the specimen basis.

Consideration of the outlined aspects has led to following discretized Tait–Bryan angles for possible specimen orientations: $\psi = \{0°, \pm 45°, \pm 135°, 180°\}$, $\theta = \{0°, -45°\}$, $\varphi = \{0°, \pm 45°, 90°\}$, allowing to manufacture a batch of specimens containing all possible combinations of ψ and θ. Adding a further cylinder with axis normal to the build plate completes the batch of 17 specimens as shown in Fig. 4.

The angle φ for each specimen is selected by evaluation of the minimum condition number resulting from the system of 21 most suitable linear equations, generated by the complete batch of specimens, whereas the other frequencies can be used for validation of the result.

Several specimen orientations and the selection of equations for the system of linear equations are specified by considerations for the estimation of certain components of the compliance tensor with respect to the reference basis.

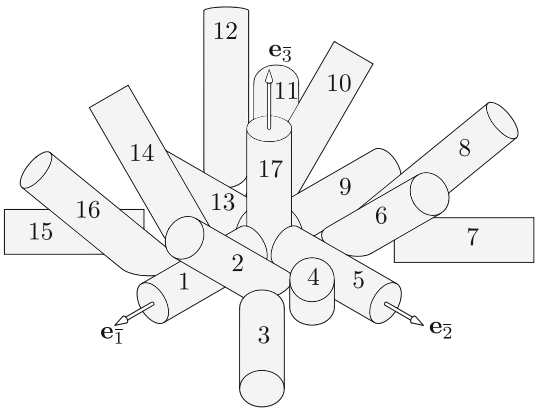

Fig. 4 Batch of specimens to be built by additive manufacturing

Specimens oriented coaxially to the basis vectors, as shown in Fig. 5, allow to directly estimate the elements on the diagonal of the matrix $\left[S_{\overline{I}\,\overline{J}}\right]$, see Eq. (13). The compliances $S_{\overline{1}}$, $S_{\overline{7}}$ and $S_{\overline{12}}$ are determined by the fundamental flexural eigenfrequencies $f_{\mathrm{f}}^{(p)}$, whereas the components $S_{\overline{16}}$, $S_{\overline{19}}$ and $S_{\overline{21}}$ are calculated from the fundamental torsional frequencies $f_{\mathrm{t}}^{(p)}$ of specimens 1, 5 and 17. In Table 2, the Tait–Bryan angles are outlined together with the corresponding nonzero transformation coefficients of sets $a_{1\,\overline{\beta}}^{(p)}$ and $a_{21\,\overline{\beta}}^{(p)}$ that contribute six equations to the system of linear equations.

The components $S_{\overline{2}}$, $S_{\overline{3}}$ and $S_{\overline{8}}$ in the left upper quadrant of $\left[S_{\overline{I}\,\overline{J}}\right]$ are estimated by the fundamental torsional frequencies of specimens 10, 14 and 15 in combination with the already determined elements on the diagonal. Their specimen planes are parallel to the coordinate planes of the reference system, but the angle between the basis vectors in the coordinate planes is 45° , as shown in Fig. 6, which leads to the sets of transformation coefficients listed in Table 3.

Three further specimens are intended to determine the components $S_{\overline{17}}$, $S_{\overline{18}}$ and $S_{\overline{20}}$ in the right lower quadrant of the matrix $\left[S_{\overline{I}\,\overline{J}}\right]$. Their specimen planes are tilted at an angle of 45° to the coordinate planes as

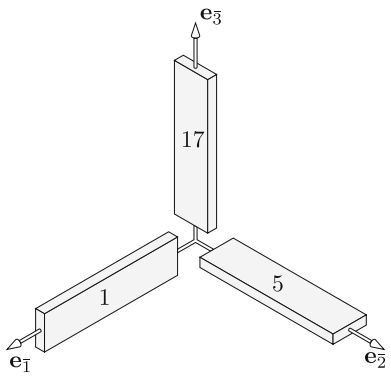

Fig. 5 Orientations of specimens 1, 5 and 17

Table 2 Orientation angles and nonzero transformation coefficients of specimens 1, 5 and 17

p	ψ (°)	θ (°)	φ (°)	$a_{1\,\overline{\beta}}^{(p)}$	$a_{21\,\overline{\beta}}^{(p)}$
1	0	0	90	$a_{1\,\overline{1}}^{(1)} = 1$	$a_{21\,\overline{19}}^{(1)} = 1$
5	90	0	0	$a_{1\,\overline{7}}^{(5)} = 1$	$a_{21\,\overline{21}}^{(5)} = 1$
17	0	− 90	0	$a_{1\,\overline{12}}^{(17)} = 1$	$a_{21\,\overline{16}}^{(17)} = 1$

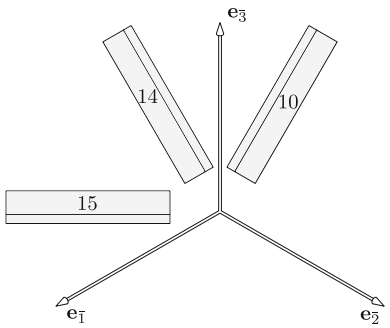

Fig. 6 Orientations of specimens 10, 14 and 15

Table 3 Orientations and nonzero transformation coefficients of specimens 10, 14 and 15

p	ψ (°)	θ (°)	φ (°)	$a_{21\,\bar{\beta}}^{(p)}$
10	180	− 45	90	$a_{21\,\bar{1}}^{(10)} = a_{21\,\overline{12}}^{(10)} = 0.25, a_{21\,\bar{3}}^{(10)} = -0.5$
14	− 90	− 45	90	$a_{21\,\bar{7}}^{(14)} = a_{21\,\overline{12}}^{(14)} = 0.25, a_{21\,\bar{8}}^{(14)} = -0.5$
15	− 45	0	0	$a_{21\,\bar{1}}^{(15)} = a_{21\,\bar{7}}^{(15)} = 0.25, a_{21\,\bar{2}}^{(15)} = -0.5$

shown in Fig. 7. An analysis of the nonzero transformation coefficients $a_{21\,\bar{\beta}}^{(p)}$ for specimens 2, 3 and 6 in Table 4 shows that these components ($S_{\overline{17}}$, $S_{\overline{18}}$ and $S_{\overline{20}}$) can be identified in combination with the already determined diagonal elements.

From the orientation selection of the first nine specimens twelve equations result, allowing to determine the elements in the abovementioned quadrants of the matrix $\left[S_{\bar{I}\,\bar{J}}\right]$ as independently as possible. Nine additional

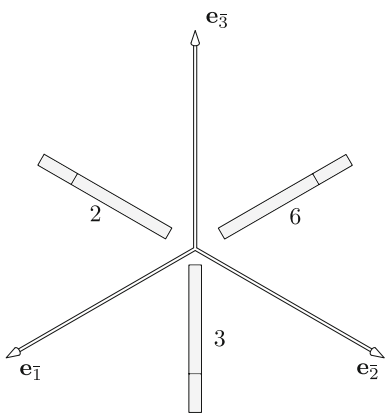

Fig. 7 Orientation of specimens 2, 3 and 6

Table 4 Orientations and nonzero transformation coefficients for specimens 2, 3 and 6

p	ψ (°)	θ (°)	φ (°)	$a_{21\,\bar{\beta}}^{(p)}$
2	0	− 45	0	$a_{21\,\overline{16}}^{(2)} = a_{21\,\overline{21}}^{(2)} = 0.5, a_{21\,\overline{18}}^{(2)} = 1$
3	45	0	90	$a_{21\,\overline{16}}^{(3)} = a_{21\,\overline{19}}^{(3)} = 0.5, a_{21\,\overline{17}}^{(3)} = 1$
6	90	− 45	0	$a_{21\,\overline{19}}^{(6)} = a_{21\,\overline{21}}^{(6)} = 0.5, a_{21\,\overline{20}}^{(6)} = 1$

Table 5 Orientations and sets of transformation coefficients for the determination of elements in the right upper square of $\left[S_{\bar{I}\,\bar{J}}\right]$

p	ψ (°)	θ (°)	φ (°)	$a^{(p)}_{\alpha\,\bar{\beta}}$
2	0	− 45	0	$a^{(2)}_{1\,\bar{\beta}}$
4	45	− 45	− 45	$a^{(4)}_{21\,\bar{\beta}}$
7	135	0	− 45	$a^{(7)}_{1\,\bar{\beta}}, a^{(7)}_{21\,\bar{\beta}}$
8	135	− 45	− 45	$a^{(8)}_{21\,\bar{\beta}}$
11	− 135	0	− 45	$a^{(11)}_{21\,\bar{\beta}}$
12	− 135	− 45	− 45	$a^{(12)}_{21\,\bar{\beta}}$
14	− 90	− 45	90	$a^{(14)}_{1\,\bar{\beta}}$
16	− 45	− 45	− 45	$a^{(16)}_{21\,\bar{\beta}}$

Table 6 Orientations of specimens for verification of the result

p	ψ (°)	θ (°)	φ (°)
9	180	0	− 45
13	− 90	0	45

equations are necessary in order to reach the full rank of 21 of the matrix $\left[M_{i\,\bar{\beta}}\right]$. It is challenging to identify orientations of further specimens, such that elements in the right upper quadrant of $\left[S_{\bar{I}\,\bar{J}}\right]$ are determinable independently from each other. Hence, the minimum condition number resulting from batches of specimen with all possible combinations of φ for the remaining 8 specimens are compared in order to find the combination of the most suitable angles and the best selection of equations in order to complete the linear system of equations. In Table 5, the resulting angles are listed together with the sets of transformation coefficients that contribute the missing nine equations, whereby the orientations of specimens 2 and 14 were already chosen by the considerations mentioned before. Following this approach, a condition number of $\kappa_2 = 8.33$ is achieved. Orientations of specimens that do not contribute to the system of linear equations are arbitrarily chosen for verification of the result. In Table 6, the orientations of these specimens are listed.

3.3 Identification of the elasticity tensor by optimization

The discrepancy between the first approximation of the compliance tensor and the exact solution of the inverse problem results from the shortcomings described in Sect. 2.3. In order to eliminate the impact of these shortcomings on the determined elasticity tensor, an optimization scheme based on the Newton–Raphson method is applied. By the proposed considerations, outlined in Sect. 3.2, 21 eigenfrequencies were already selected allowing a robust identification of the compliance tensor. In the optimization scheme the sum of least squared differences between these eigenfrequencies, calculated by the numerical modal analysis on the basis of the current compliance tensor and the corresponding measured ones, is minimized. This results in the following optimization problem:

$$\min_{[S_{\bar{\alpha}}]} g = \min \frac{1}{2} \left|\left|\left[f_i^{\mathrm{FEM}}\right] - \left[f_i^{\mathrm{Ex}}\right]\right|\right|^2. \tag{24}$$

The vector $\left[f_i^{\mathrm{FEM}}\right]$ contains the selected eigenfrequencies of type $f_{\mathrm{f}}^{(p)}$ or $f_{\mathrm{t}}^{(p)}$ determined by the numerical modal analysis and the vector $\left[f_i^{\mathrm{Ex}}\right]$ represents the corresponding measured eigenfrequencies.

The gradient of the objective function g results from the deviation between the frequencies:

$$\left[\frac{\partial g}{\partial S_{\bar{\alpha}}}\right] = \left[f_i^{\mathrm{FEM}}\right] - \left[f_i^{\mathrm{Ex}}\right], \tag{25}$$

whereas the partial derivatives in the Hessian are approximated by the forward difference quotients, similar to the approach in Eq. (10), but with respect to the components corresponding to the reference basis:

$$\left[\frac{\partial f_i}{\partial S_{\bar{\alpha}}}\right] = \begin{bmatrix} \frac{\partial f_1}{\partial S_{\bar{1}}} & \frac{\partial f_1}{\partial S_{\bar{2}}} & \cdots & \frac{\partial f_1}{\partial S_{\bar{21}}} \\ \frac{\partial f_2}{\partial S_{\bar{1}}} & \frac{\partial f_2}{\partial S_{\bar{2}}} & \cdots & \frac{\partial f_2}{\partial S_{\bar{21}}} \\ \vdots & \vdots & \cdots & \vdots \\ \frac{\partial f_{21}}{\partial S_{\bar{1}}} & \frac{\partial f_{21}}{\partial S_{\bar{2}}} & \cdots & \frac{\partial f_{21}}{\partial S_{\bar{21}}} \end{bmatrix}. \tag{26}$$

In each iteration step, the optimization variables are updated:

$$[S_{\bar{\alpha}}]_{\{n+1\}} = [S_{\bar{\alpha}}]_{\{n\}} - \left(\left[\frac{\partial f_i^{\mathrm{FEM}}}{\partial S_{\bar{\alpha}}}\right]_{\{n\}}\right)^{-1} \cdot \left[\frac{\partial g}{\partial S_{\bar{\alpha}}}\right]_{\{n\}}. \tag{27}$$

It is assumed that by the aforementioned choice of specimen orientations and selection of eigenfrequencies for the optimization scheme, the objective function g has a single root, which is found by using the approximated compliance tensor as starting point for the optimization problem.

The proposed approach is validated by assuming a certain compliance tensor with respect to the reference basis, which is based on different material models and numerically calculating the corresponding eigenfrequencies of the specimens. Subsequently, the approximation of the compliance tensor and the optimization scheme is executed. These studies showed convergency to the assumed compliance tensor for all investigated material models, based on the single-crystal elastic properties of IN718, as shown in Table 8, even in single crystalline state and adverse orientation of planes of material symmetry.

4 Experimental

In order to verify the proposed method, the batch of specimens described in Sect. 3.2 was manufactured by SLM. In the applied scanning strategy, the scan vectors are rotated in every layer by 67°, but directions within a certain range of parallelism to the inert gas flow are skipped. Due to the variety in the orientation of the scan vectors over all layers, neither the symmetry class nor the orientation of possible planes of symmetry of the macroscopic elasticity tensor is known a priori. The required high geometric accuracy of the specimens is achieved by electrical discharge machining (EDM) of the specimens from the built cylinders. Due to the residual stresses induced during the additive manufacturing process, the specimens are distorted during machining, which is corrected in subsequent recutting steps in order to achieve a low deviation in parallelism of the specimen sides. The dimensions of each specimen are measured by a micrometer screw at several positions and additionally the mass is determined accurately, allowing to set up a calculation model of each individual specimen for the equations in closed form, as well as for the finite element model. The parameters for the calculation models are given in Table 9 of "Appendix B". The fundamental eigenfrequencies are measured by employing an experimental setup similar to the one described by Roebben [2]. Table 7 summarizes the measured eigenfrequencies of all specimens.

4.1 Results

The first approximation of the elasticity tensor results from the inverse of the approximated compliance tensor, as described in Sect. 3.1, and is presented in Voigt notation:

$$\left[C_{\bar{I}\,\bar{J}}\right]_{\{0\}} = \begin{bmatrix} 277 & 117 & 104 & -14 & 3 & 2 \\ & 257 & 120 & -7 & 2 & 9 \\ & & 260 & -10 & -1 & 8 \\ & & & 85 & 2 & 2 \\ & \mathrm{sym} & & & 68 & 0 \\ & & & & & 73 \end{bmatrix} \mathrm{GPa}.$$

Table 7 Comparison of experimentally determined flexural and torsional eigenfrequencies $f_{\mathrm{f}}^{\mathrm{Ex}}$ and $f_{\mathrm{t}}^{\mathrm{Ex}}$ with the predicted frequencies determined numerically, based on the approximated elasticity tensor $\left[C_{\bar{I}\bar{J}}\right]_{\{0\}}$ and the elasticity tensor subsequently to the last iteration of the optimization scheme $\left[C_{\bar{I}\bar{J}}\right]_{\{3\}}$

p	$f_{\mathrm{f}}^{\mathrm{Ex}}$ $(10^3\mathrm{Hz})$	$f_{\mathrm{f}\{0\}}^{\mathrm{FEM}}$ $(10^3\mathrm{Hz})$	$f_{\mathrm{f}\{3\}}^{\mathrm{FEM}}$ $(10^3\mathrm{Hz})$	$f_{\mathrm{t}}^{\mathrm{Ex}}$ $(10^3\mathrm{Hz})$	$f_{\mathrm{t}\{0\}}^{\mathrm{FEM}}$ $(10^3\mathrm{Hz})$	$f_{\mathrm{t}\{3\}}^{\mathrm{FEM}}$ $(10^3\mathrm{Hz})$
1	5472*	5466	5472	9924*	10013	9924
2	5048*	5063	5049	10799*	10833	10799
3	5208	5300	5252	10576*	10592	10576
4	5318	5280	5355	10153*	10290	10153
5	5074*	5085	5074	10247*	10364	10247
6	5553	5404	5495	10080*	10135	10079
7	5163*	5162	5163	10518*	10571	10518
8	5317	5057	5041	10925*	10890	10925
9	5447	5468	5475	10084	10125	10051
10	5068	5064	5006	10911*	10888	10911
11	5163	5305	5256	10596*	10607	10597
12	5308	5417	5377	10058*	10155	10058
13	5079	5072	5062	10429	10776	10744
14	5586*	5578	5586	9991*	10064	9991
15	5152	5152	5154	10331*	10402	10331
16	5291	5287	5250	10871*	10814	10871
17	5221*	5228	5221	11035*	10947	11035

Frequencies that contribute to the optimization scheme are marked by *

Subsequently, three optimization steps are applied, as described in Sect. 3.3, which leads to the elasticity tensor:

$$\left[C_{\bar{I}\,\bar{J}}\right]_{\{3\}} = \begin{bmatrix} 284 & 127 & 108 & -11 & 8 & 4 \\ & 265 & 128 & -4 & 7 & 10 \\ & & 265 & -8 & 1 & 12 \\ & & & 87 & 1 & 2 \\ & \mathrm{sym} & & & 67 & 1 \\ & & & & & 71 \end{bmatrix} \mathrm{GPa}.$$

Table 7 shows a comparison between the experimentally determined eigenfrequencies of all specimens and the corresponding ones predicted numerically on the basis of the approximated compliance tensor subsequently to the third iteration step.

4.2 Analysis of the frequency deviations

The good agreement of the measured eigenfrequencies that do not contribute to the determination of the elasticity tensor with the corresponding ones predicted on the basis of the resulting elasticity tensor (Table 7) indicate the validity the result. The maximum deviation in the fundamental flexural frequency is 276 Hz, whereas the maximum deviation in the fundamental torsional frequency is 315 Hz. On the basis of the elasticity tensor, determined by optimization, it is possible to express the frequency deviation in form of a deviation in the Young's modulus ΔE_1 and shear modulus ΔG_{12} by linear approximations:

$$\left|\Delta E_1\right| = \frac{\left|f_{\mathrm{f}}^{\mathrm{Ex}} - f_{\mathrm{f}\{3\}}^{\mathrm{FEM}}\right|}{\left.\frac{\partial f^{\mathrm{FEM}}}{\partial E_1}\right|_{\left[C_{\bar{I}\,\bar{J}}\right]_{\{3\}}}}, \tag{28}$$

$$\left|\Delta G_{12}\right| = \frac{\left|f_{\mathrm{t}}^{\mathrm{Ex}} - f_{\mathrm{t}\{3\}}^{\mathrm{FEM}}\right|}{\left.\frac{\partial f^{\mathrm{FEM}}}{\partial G_{12}}\right|_{\left[C_{\bar{I}\,\bar{J}}\right]_{\{3\}}}}, \tag{29}$$

resulting in the maximum absolute deviations of $|\Delta E_1| = 20\,\mathrm{GPa}$ and $|\Delta G_{12}| = 5\,\mathrm{GPa}$.

4.3 Analysis of the determined elasticity tensor

The Voigt tensor V_{ij} and the dilatational modulus D_{ij} provide further information on the elastic behavior and can be directly calculated from the elasticity tensor.

The dilatational modulus $D_{ij} = C_{ijkk}$ is calculated by contraction of the elasticity tensor with respect to the last two indices. In case of the elastic behavior of a cubic single crystal, the dilatational modulus is a spherical tensor and can be directly expressed by the elastic constants [15]:

$$D_{ij} = d\,\delta_{ij}, \qquad \text{where} \qquad d = C_{1111} + 2\,C_{1122}. \tag{30}$$

The interpretation of the elasticity tensor as a tensor of second order in a six-dimensional space with an orthogonal basis by application of the Mandel notation allows a representation of the elasticity tensor and the compliance tensor in form of a spectral decomposition involving six eigenvalues λ_i with corresponding orthogonal eigenvectors $\underline{\mathbf{N}}_i$ [16]:

$$\underline{\underline{\mathbf{C}}} = \sum_{i=1}^{6} \lambda_i\, \underline{\mathbf{N}}_i \otimes \underline{\mathbf{N}}_i, \tag{31}$$

$$\underline{\underline{\mathbf{S}}} = \sum_{i=1}^{6} \frac{1}{\lambda_i}\, \underline{\mathbf{N}}_i \otimes \underline{\mathbf{N}}_i. \tag{32}$$

The eigenvectors can be transformed to second-order tensors in the original three-dimensional space. Analysis of the spectral decomposition of the elasticity tensor of a cubic single crystal shows that the eigenvalue λ_1, corresponding to the compression mode, correlates with the diagonal elements of the dilatational modulus:

$$\lambda_1 = d = C_{1111} + 2\,C_{1122}. \tag{33}$$

Hence, due to the orthogonality of the eigenvectors, the compression mode is decoupled from the shear modes. Consequently, in case of cubic crystals, the bulk moduli of single crystals and polycrystals are identical and independent of the homogenization theory. This is also reflected by the formulas in closed form suggested by Böhlke et al. [17,18] for the homogenization by Voigt, Reuss and the singular approximation of the Hashin–Shtrikman bounds. These relationships allow to compare the diagonal elements of the dilatational modulus calculated from the determined elasticity tensor,

$$\left[D_{\bar{I}\bar{J}}\right]_{\{3\}} = \begin{bmatrix} 519 & 26 & 16 \\ & 520 & -24 \\ \text{sym} & & 501 \end{bmatrix} \text{GPa},$$

with those calculated from single-crystal data taken from the literature, as listed in Table 8. It can be seen that the diagonal elements of $\left[D_{\bar{I}\bar{J}}\right]_{\{3\}}$ are almost identical and show a good agreement with the literature. The low deviatoric part of the dilatational modulus is a further indication of the validity of the result.

The Voigt tensor $V_{ij} = C_{ikkj}$ is calculated by the contraction of the elasticity tensor with respect to the middle indices. In case of cubic single crystals, the Voigt tensor is spherical and depends on the elastic constants:

$$V_{ij} = v\,\delta_{ij}, \qquad \text{where} \qquad v = C_{1111} + 2\,C_{1212}. \tag{34}$$

In contrast to the dilatational modulus the Voigt tensor of orientation averaged elasticity tensors is only spherical by application of the orientation average suggested by Voigt. Nevertheless, the Voigt tensor of the determined elasticity tensor shows also small values of the off-diagonal elements:

$$\left[V_{\bar{I}\bar{J}}\right]_{\{3\}} = \begin{bmatrix} 422 & 15 & 11 \\ & 423 & -12 \\ \text{sym} & & 418 \end{bmatrix} \text{GPa}.$$

The diagonal elements are close to each other, but slightly lower compared to the corresponding ones reported in the literature, as outlined in Table 8.

Table 8 Elastic constants of single crystals of IN718 with corresponding diagonal elements of the dilatational modulus and the Voigt tensor

Refs.	[20]	[21]	[22]	[23]
C_{1111} (GPa)	240.9	259.6	231.2	244.8
C_{1122} (GPa)	140.5	179.0	145.1	149.2
C_{1212} (GPa)	105.7	109.6	117.2	123.6
d (GPa)	521.9	617.6	521.4	543.2
v (GPa)	452.3	478.8	465.6	492.0
H (GPa)	95.1	105.0	96.8	96.8
h (GPa)	23.2	46.3	18.6	18.6

The harmonic decomposition provides a further possibility to analyze the determined elasticity tensor. It represents a decomposition of totally symmetric tensors of even order into harmonic tensors, as described by Baerheim [19] for application to the elasticity tensor. In a first step, the elasticity tensor is split up into a totally symmetric tensor M_{ijkl} and an asymmetric tensor of fourth order A_{ijkl}, according to:

$$M_{ijkl} = \frac{1}{3}\left(C_{ijkl} + C_{ikjl} + C_{iljk}\right), \tag{35}$$

$$A_{ijkl} = C_{ijkl} - M_{ijkl}. \tag{36}$$

The totally symmetric part is described by three harmonic tensors: A scalar value H, a second-order harmonic tensor H_{ij} and a harmonic tensor of fourth order H_{ijkl}:

$$M_{ijkl} = H_{ijkl} + \delta_{ij}\,H_{kl} + \delta_{kl}\,H_{ij} + \delta_{ik}\,H_{jl} + \delta_{jl}\,H_{ik} + \delta_{il}\,H_{jk} + \delta_{jk}\,H_{il} + H\left(\delta_{ij}\,\delta_{jk} + \delta_{ik}\,\delta_{jl} + \delta_{il}\,\delta_{jk}\right). \tag{37}$$

The asymmetric part can be described by a linear map of a second-order symmetric tensor h_{ij} and a scalar value h, according to:

$$A_{ijkl} = \delta_{ij}\,h_{kl} + \delta_{kl}\,h_{ij} - \frac{1}{2}\left(\delta_{ik}\,h_{jl} + \delta_{jl}\,h_{ik} + \delta_{il}\,h_{jk} + \delta_{jk}\,h_{il}\right) + h\left(\delta_{ij}\,\delta_{kl} - \frac{1}{2}\,\delta_{ik}\,\delta_{jl} - \frac{1}{2}\,\delta_{il}\,\delta_{jk}\right). \tag{38}$$

The scalar values H and h depend on the trace of the Voigt tensor and the dilatational modulus:

$$H = \frac{1}{45}\left(D_{kk} + 2\,V_{kk}\right), \tag{39}$$

$$h = \frac{1}{9}\left(D_{kk} - V_{kk}\right), \tag{40}$$

whereby the second-order harmonic tensors can be described by their deviators $\hat{D}_{ij}$ and $\hat{V}_{ij}$:

$$H_{ij} = \frac{1}{21}\left(\hat{D}_{ij} + 2\,\hat{V}_{ij}\right), \tag{41}$$

$$h_{ij} = \frac{2}{3}\left(\hat{D}_{ij} - \hat{V}_{ij}\right). \tag{42}$$

Since the harmonics H and h are invariant for cubic single crystals and hence also for polycrystals by application of the orientation average by Voigt, these quantities of the determined elasticity tensor can be compared with the corresponding ones of the single-crystal data from the literature listed in Table 8. For the determined elasticity tensor the harmonics result to $H_{\{3\}} = 90.41\,\text{GPa}$ and $h_{\{3\}} = 30.86\,\text{GPa}$, which are in range of the data reported in the literature. The application of the orientation average by Voigt would lead to zeros of the second-order harmonic tensors, in case of polycrystalline cubic alloys, as the deviators of the Voigt tensor and the dilatational modulus are zero in this case. Hence, theoretically the number of independent constants for the description of the elasticity tensor is reduced from 21 to 11, as harmonic tensors of second order can be described by 5 independent constants [24]. However, the Voigt orientation average is a rough

estimate of the resulting elasticity tensor of a polycrystal. The components of the harmonic tensors of second order corresponding to the determined elasticity tensors show low values:

$$\left[H_{\bar{I}\bar{J}}\right]_{\{3\}} = \begin{bmatrix} 0.38 & 2.64 & 1.79 \\ & 0.48 & -2.23 \\ \text{sym} & & -0.86 \end{bmatrix} \text{GPa},$$

$$\left[h_{\bar{I}\bar{J}}\right]_{\{3\}} = \begin{bmatrix} 3.02 & 7.05 & 3.53 \\ & 3.29 & -8.05 \\ \text{sym} & & -6.30 \end{bmatrix} \text{GPa},$$

which confirms this aspect.

Finally the question arises, if the determined elasticity tensor can be assigned to any certain symmetry class. Due to measurement deviations and the determination of all 21 independent components of the elasticity tensor an exact assignment is not possible, except to the triclinic symmetry class. Therefore, an appropriate distance measure to symmetry classes as proposed by Stahn et al. [25], which is based on the contribution of Francois et al. [26] is used. In a first step, the components of the elasticity tensor are transformed to a symmetry basis, which is found by eigenvectors of the dyad:

$$\underline{\underline{\mathbf{t}}} = \underline{\underline{\mathbf{h}}} + \frac{h}{2}\underline{\underline{\mathbf{1}}}, \tag{43}$$

where $\underline{\underline{\mathbf{h}}}$ and h are the harmonic tensors, as described above. This allows to calculate the closest elasticity tensor of the symmetry class $\mathcal{G}$ by the average of the orbit of the elasticity tensor in the corresponding symmetry group, according to:

$$\mathbb{C}_{\mathcal{G}} = \frac{1}{|\mathcal{G}|}\sum_{i=1}^{|\mathcal{G}|}\underline{\underline{\mathbf{Q}}}_i * \mathbb{C}, \tag{44}$$

where $\mathbb{C}$ denotes the fourth-order elasticity tensor to be analyzed in the symmetry basis, $\underline{\underline{\mathbf{Q}}}_i \in \mathcal{G}$ are the elements of the corresponding symmetry group, $*$ is the Rayleigh product and $|\cdot|$ denotes the cardinality. The normalized distance of the elasticity tensor to the closest element of the symmetry class is calculated by:

$$d\left(\mathbb{C}, \mathcal{G}\right) = \frac{\left|\left|\mathbb{C} - \mathbb{C}_{\mathcal{G}}\right|\right|}{\left|\left|\mathbb{C}\right|\right|}, \tag{45}$$

where $\left|\left|\cdot\right|\right|$ denotes the Frobenius norm.

Figure 8 presents a comparison between the distances of both the determined elasticity tensor and the elasticity tensor of the cubic single crystal of IN718 reported in the literature [19] to different non-triclinic symmetry classes. Apparently, none of the distances of the determined elasticity tensor to any of the symmetry classes is particularly small. An interesting fact is that its distance to the cubic symmetry class is almost equal to its distance to the isotropic class, even though the single crystals of the polycrystalline aggregate are cubic. Furthermore, the distance of the elasticity tensor describing the elastic behavior of the cubic single crystal to the isotropic class is twice the distance of the determined elasticity tensor to this class. Hence, the determined elasticity tensor marks the halfway stage of the microstructure on its way from the single crystalline state to an untextured polycrystalline aggregate. The closest elasticity tensor of the isotropic class to the determined elasticity tensor is specified by a Young's modulus of 196 GPa and a shear modulus 75 GPa.

5 Discussion

The presented method was demonstrated on a batch of specimens from the nickel-base alloy IN718 fabricated by SLM. An analysis of the results indicates the validity of the determined elasticity tensor. The orientations and the geometry of the specimens were conceived with the objectives that the method is stable with respect to measurement deviations and converges for a wide range of various types of macroscopic elastic anisotropy.

Numerical verifications involving different material models confirm that the proposed method converges, even in case of the nickel-base alloy in single crystalline state and adverse orientation of the planes of material

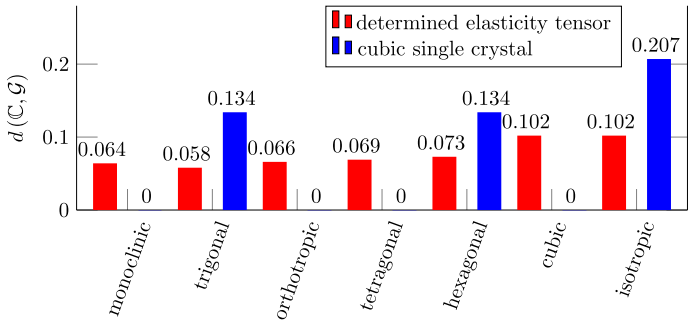

Fig. 8 Comparison of the distances of the determined elasticity tensor and the elasticity tensor of the cubic single crystal (of IN718 reported in the literature [19]), to different non-triclinic symmetry classes

symmetry. The application of the proposed method to materials with stronger anisotropy may lead to divergence in the Newton–Raphson optimization scheme, which could be avoided using alternative optimization strategies. However, as a consequence of stronger anisotropy, the reliability of the estimations in closed form declines. Therefore, the choice of specimen orientations may get unfavorable, leading to an increased impact of the measurement deviations on the results.

The determination of the elasticity tensor is based on the assumption of homogeneous elastic behavior, which is reasonable for the determination of the elastic properties of bulk materials, but leads to additional uncertainties in case of inhomogeneous elastic behavior.

In contrast to a texture-based approach to assess the elasticity tensor of polycrystalline materials, the presented method does not require the knowledge of the elastic constants of the corresponding single crystal. The elastic properties determined by the proposed method are averaged over a large volume compared to diffraction measurements, such as EBSD (electron backscatter diffraction) or XRD (X-ray diffraction). This is particularly beneficial in case of additively manufactured alloys, where the grain size can be large and only a few layers are captured by the diffraction measurements.

Besides modeling uncertainties, such as the assumption of homogeneity and the neglect of material damping, as well as the effect of residual stresses on the vibration behavior, the accuracy of the proposed method mainly depends on the deviation of the specimen dimensions in the calculation models from the geometry of the manufactured specimens. In particular, a discrepancy in specimen thickness shows the strongest influence. An increased specimen thickness lowers the sensitivity of the eigenfrequencies with respect to thickness variations and additionally leads to a more reliable specimen preparation.

On the other hand, with increasing specimen thickness the estimations in closed form become less accurate due to the increasing influence of S_{1313}, as discussed in Sect. 2.3, and the sensitivity with respect to the elastic properties decreases. The chosen specimen geometry represents a good balance between these aspects.

In case of cubic single-phase alloys, the second-order harmonic tensors of the elasticity tensor are zero on the assumption of the orientation average by Voigt. Therefore, a further development of the proposed method enabling a robust determination of the harmonics of the elasticity tensor seems to be promising in order to reduce the number of required specimens.

6 Conclusion

In this contribution, a method was suggested to determine the anisotropic elasticity tensor from the eigenfrequencies of a batch of specimens by the impulse excitation technique. It allows an efficient and reliable identification of the elastic properties, without requiring additional information on the microscopic scale. Hence, it is a valuable tool to explore the relation between the scanning strategy in the SLM-process and the resulting anisotropic elastic behavior, provided the microstructure is homogeneous on the macroscopic level. In this context, a further verification by studies on different SLM-processed materials in combination with microstructural investigations is necessary. The knowledge of the anisotropic elasticity tensor is also essential for a reliable estimation of the residual stresses on the macroscopic level, which play a crucial role in SLM-processing.

Since the impulse excitation technique can also be employed at elevated temperatures, a study of the evolution of the anisotropic elasticity tensor during heat treatment seems to be feasible, providing valuable information for the further development of the SLM-based material processing route.

Funding Open Access funding enabled and organized by Projekt DEAL.

Declarations

Conflict of interest The authors declare that they have no conflict of interest.

Appendix A: Transformation of the compliance tensor

According to the transformation rule for a fourth-order tensor, an arbitrary component S_{ijkl} with respect to the specimen basis is determined by the sum of 81 components with respect to the reference basis multiplied with the corresponding transformation coefficients:

$$S_{i\,j\,k\,l} = S_{\bar{m}\,\bar{n}\,\bar{o}\,\bar{p}}\; Q_{i\,\bar{m}}\, Q_{j\,\bar{n}}\, Q_{k\,\bar{m}}\, Q_{l\,\bar{p}} = S_{\bar{1}\bar{1}\bar{1}\bar{1}}\, Q_{i\,\bar{1}}\, Q_{j\,\bar{1}}\, Q_{k\,\bar{1}}\, Q_{k\,\bar{1}} + \cdots + S_{\bar{3}\bar{3}\bar{3}\bar{3}}\, Q_{i\,\bar{3}}\, Q_{j\,\bar{3}}\, Q_{k\,\bar{3}}\, Q_{k\,\bar{3}} \quad (46)$$

The minor and major symmetries of the compliance tensor allow permutations of the tensor indices, as described in Sect. 2. Depending on the choice of the indices, these permutations lead to several equivalent components that can be grouped together. The following types of groups can be distinguished:

- $S_{\langle i\rangle\langle i\rangle\langle i\rangle\langle i\rangle}$
- $S_{\langle i\rangle\langle i\rangle\langle j\rangle\langle j\rangle} = S_{\langle j\rangle\langle j\rangle\langle i\rangle\langle i\rangle}$
- $S_{\langle i\rangle\langle i\rangle\langle i\rangle\langle j\rangle} = S_{\langle i\rangle\langle i\rangle\langle j\rangle\langle i\rangle} = S_{\langle i\rangle\langle j\rangle\langle i\rangle\langle i\rangle} = S_{\langle j\rangle\langle i\rangle\langle i\rangle\langle i\rangle}$
- $S_{\langle i\rangle\langle j\rangle\langle i\rangle\langle k\rangle} = S_{\langle j\rangle\langle i\rangle\langle i\rangle\langle k\rangle} = S_{\langle i\rangle\langle j\rangle\langle k\rangle\langle i\rangle} = S_{\langle j\rangle\langle i\rangle\langle i\rangle\langle k\rangle} = S_{\langle i\rangle\langle k\rangle\langle i\rangle\langle j\rangle} = S_{\langle i\rangle\langle k\rangle\langle j\rangle\langle i\rangle} = S_{\langle k\rangle\langle i\rangle\langle i\rangle\langle j\rangle} = S_{\langle k\rangle\langle i\rangle\langle j\rangle\langle i\rangle}$
- $S_{\langle i\rangle\langle j\rangle\langle i\rangle\langle j\rangle} = S_{\langle j\rangle\langle i\rangle\langle i\rangle\langle j\rangle} = S_{\langle i\rangle\langle j\rangle\langle j\rangle\langle i\rangle} = S_{\langle j\rangle\langle i\rangle\langle j\rangle\langle i\rangle}$.

These permutations allow to reduce the transformation from 81 summands to 21 summands of independent components with corresponding adapted transformation coefficients, that include the transformation coefficients of equivalent components, as shown in the following transformation, where an independent component of each type of group is shown in detail:

$$\begin{aligned}
S_{ijkl} = {} & S_{\bar{1}\bar{1}\bar{1}\bar{1}}\, Q_{i\,\bar{1}}\, Q_{j\,\bar{1}}\, Q_{k\,\bar{1}}\, Q_{l\,\bar{1}} + S_{\bar{1}\bar{1}\bar{2}\bar{2}} \left(Q_{i\,\bar{1}}\, Q_{j\,\bar{1}}\, Q_{k\,\bar{2}}\, Q_{l\,\bar{2}} + Q_{i\,\bar{2}}\, Q_{j\,\bar{2}}\, Q_{k\,\bar{1}}\, Q_{l\,\bar{1}} \right) \\
& + S_{\bar{1}\bar{1}\bar{1}\bar{2}} \left(Q_{i\,\bar{1}}\, Q_{j\,\bar{1}}\, Q_{k\,\bar{1}}\, Q_{l\,\bar{2}} + Q_{i\,\bar{1}}\, Q_{j\,\bar{1}}\, Q_{k\,\bar{2}}\, Q_{l\,\bar{1}} + Q_{i\,\bar{1}}\, Q_{j\,\bar{2}}\, Q_{k\,\bar{1}}\, Q_{l\,\bar{1}} + Q_{i\,\bar{2}}\, Q_{j\,\bar{1}}\, Q_{k\,\bar{1}}\, Q_{l\,\bar{2}} \right) \\
& + S_{\bar{1}\bar{2}\bar{1}\bar{3}} \left(Q_{i\,\bar{1}}\, Q_{j\,\bar{2}}\, Q_{k\,\bar{1}}\, Q_{l\,\bar{3}} + Q_{i\,\bar{2}}\, Q_{j\,\bar{1}}\, Q_{k\,\bar{1}}\, Q_{l\,\bar{3}} + Q_{i\,\bar{1}}\, Q_{j\,\bar{2}}\, Q_{k\,\bar{3}}\, Q_{l\,\bar{1}} + Q_{i\,\bar{2}}\, Q_{j\,\bar{1}}\, Q_{k\,\bar{3}}\, Q_{l\,\bar{1}} + \right. \\
& \left. + Q_{i\,\bar{1}}\, Q_{j\,\bar{3}}\, Q_{k\,\bar{1}}\, Q_{l\,\bar{2}} + Q_{i\,\bar{1}}\, Q_{j\,\bar{3}}\, Q_{k\,\bar{2}}\, Q_{l\,\bar{1}} + Q_{i\,\bar{3}}\, Q_{j\,\bar{1}}\, Q_{k\,\bar{1}}\, Q_{l\,\bar{2}} + Q_{i\,\bar{3}}\, Q_{j\,\bar{1}}\, Q_{k\,\bar{2}}\, Q_{l\,\bar{1}} \right) \\
& + S_{\bar{1}\bar{2}\bar{1}\bar{2}} \left(Q_{i\,\bar{1}}\, Q_{j\,\bar{2}}\, Q_{k\,\bar{1}} Q_{l\,\bar{2}} + Q_{i\,\bar{2}}\, Q_{j\,\bar{1}}\, Q_{k\,\bar{1}} Q_{l\,\bar{2}} + Q_{i\,\bar{1}}\, Q_{j\,\bar{2}}\, Q_{k\,\bar{2}} Q_{l\,\bar{1}} + Q_{i\,\bar{2}}\, Q_{j\,\bar{1}}\, Q_{k\,\bar{2}} Q_{l\,\bar{1}} \right) \\
= {} & S_{\bar{1}}\, a_{i\,\bar{1}} + \cdots + S_{\bar{2}}\, a_{i\,\bar{2}} + \cdots + S_{\bar{6}}\, a_{i\,\bar{6}} + S_{\bar{20}}\, a_{i\,\bar{20}} + \cdots + S_{\bar{21}}\; a_{i\,\bar{21}}.
\end{aligned} \quad (47)$$

Appendix B: Model parameters

The average dimensional values of the specimens result from single measurements by a micrometer screw at 13 positions for thickness t, 5 positions for width b and 3 positions for length l. The density ρ is calculated from the dimensions and the determined mass of the specimen.

Table 9 Average dimensional values, masses and calculated densities of the specimens

p	l (mm)	b (mm)	t (mm)	m (g)	$\rho\,(\mathrm{g\,cm^{-3}})$
1	$65.013_{(0.005)}$	$18.019_{(0.003)}$	$4.495_{(0.014)}$	42.934	8.154
2	$65.010_{(0.003)}$	$18.012_{(0.008)}$	$4.514_{(0.003)}$	43.297	8.191
3	$65.004_{(0.004)}$	$18.011_{(0.008)}$	$4.512_{(0.005)}$	43.262	8.190
4	$65.013_{(0.001)}$	$18.010_{(0.010)}$	$4.514_{(0.004)}$	43.300	8.193
5	$65.010_{(0.001)}$	$18.009_{(0.005)}$	$4.513_{(0.006)}$	43.245	8.184
6	$65.013_{(0.002)}$	$18.010_{(0.008)}$	$4.503_{(0.006)}$	43.115	8.178
7	$65.017_{(0.005)}$	$17.990_{(0.008)}$	$4.512_{(0.004)}$	43.185	8.182
8	$65.003_{(0.003)}$	$18.016_{(0.008)}$	$4.522_{(0.005)}$	43.370	8.190
9	$65.010_{(0.002)}$	$18.018_{(0.006)}$	$4.503_{(0.010)}$	43.127	8.176
10	$64.991_{(0.001)}$	$18.007_{(0.007)}$	$4.515_{(0.004)}$	43.278	8.191
11	$65.014_{(0.004)}$	$18.018_{(0.005)}$	$4.520_{(0.004)}$	43.385	8.194
12	$65.008_{(0.003)}$	$18.008_{(0.011)}$	$4.510_{(0.007)}$	43.224	8.187
13	$64.999_{(0.006)}$	$18.016_{(0.003)}$	$4.496_{(0.006)}$	43.020	8.171
14	$65.011_{(0.004)}$	$18.011_{(0.006)}$	$4.511_{(0.004)}$	43.219	8.182
15	$65.027_{(0.003)}$	$18.013_{(0.003)}$	$4.493_{(0.009)}$	42.954	8.161
16	$65.016_{(0.001)}$	$18.013_{(0.012)}$	$4.509_{(0.009)}$	43.227	8.186
17	$65.027_{(0.007)}$	$17.996_{(0.006)}$	$4.501_{(0.007)}$	43.081	8.179

The standard deviations are given in brackets

References

1. ASTM: E1876–15: Standard test method for dynamic Young's modulus, shear modulus, and Poisson ratio by impulse excitation of vibration. American Society for Testing Materials (2001). https://doi.org/10.1520/E1876-15
2. Roebben, G., Bollen, B., Brebels, A., Van Humbeeck, J., Van der Biest, O.: Impulse excitation apparatus to measure resonant frequencies, elastic moduli and internal friction at room and high temperature. Rev. Sci. Instrum. **68**, 4511–4515 (1997). https://doi.org/10.1063/1.1148422
3. Radovic, M., Lara-Curzio, E., Riester, L.: Comparison of different experimental techniques for determination of elastic properties of solids. Mat. Sci. Eng. A-Struct **368**, 56–70 (2004). https://doi.org/10.1016/j.msea.2003.09.080
4. Etcheverry, J.I., Sánchez, G.A.: Resonance frequencies of parallelepipeds for determination of elastic moduli: An accurate numerical treatment. J. Sound Vib. **321**, 631–646 (2009). https://doi.org/10.1016/j.jsv.2008.10.026
5. Lauwagie, T., Sol, H., Roebben, G., Heylen, W., Shi, Y., Van der Biest, O.: Mixed numerical–experimental identification of elastic properties of orthotropic metal plates. NDT & E Int. **36**, 487–495 (2003). https://doi.org/10.1016/S0963-8695(03)00048-3
6. Pedersen, P., Frederiksen, P.S.: Identification of orthotropic material moduli by a combined experimental/numerical method. Measurement **10**, 113–118 (1992). https://doi.org/10.1016/0263-2241(92)90003-M
7. Sol, H., Hua, H., De Visscher, J., Vantomme, J., De Wilde, W.: A mixed numerical/experimental technique for the nondestructive identification of the stiffness properties of fiber reinforced composite materials. NDT & E Int. **30**, 85–91 (1997). https://doi.org/10.1016/S0963-8695(96)00049-7
8. Lauwagie, T., Sol, H., Heylen, W., Roebben, G.: Determination of the in-plane elastic properties of the different layers of laminated plates by means of vibration testing and model updating. J. Sound Vib. **274**, 529–546 (2004). https://doi.org/10.1016/j.jsv.2003.05.023
9. Bertram, A., Han, L., Olschewski, J., Sockel, H.G.: Identification of elastic constants and orientation of single crystals by resonance measurements and FE analysis. Int. J. Comput. Appl. **7**, 284–291 (1994). https://doi.org/10.1504/IJCAT.1994.062532
10. Han, J., Bertram, A., Olschewski, J., Hermann, W., Sockel, H.G.: Identification of elastic constants of alloys with sheet and fiber textures based on resonance measurements and finite element analysis. Mat. Sci. Eng. A-Struct. **191**, 105–111 (1995). https://doi.org/10.1016/0921-5093(95)80008-5
11. Böhlke, T., Bertram, A.: The evolution of Hooke's law due to texture development in FCC polycrystals. Int. J. Solids Struct. **38**, 9437–9459 (2001). https://doi.org/10.1016/S0020-7683(01)00130-5
12. Sedlák, P., Seiner, H., Zídek, J., Janovská, M., Landa, M.: Determination of all 21 independent elastic coefficients of generally anisotropic solids by resonant ultrasound spectroscopy: Benchmark Examples. Exp. Mech. **54**, 1073–1085 (2014). https://doi.org/10.1007/s11340-014-9862-6

13. Krempaszky, C., Obermayer, T., Holfelder, P., Junghans, S., Werner, E.: Mechanics of materials: Towards predictive methods for kinetics in plasticity, fracture and damage: Anisotropic elasticity of nickel-based alloys processed by selective laser melting. Oberwolfach Rep. **17**, 748–750 (2020). https://doi.org/10.4171/OWR/2020/13
14. Leissa, A.: Vibration of Plates. Office of Technology Utilization National Aeronautics and Space Administration (1969). https://doi.org/10.1002/zamm.19710510331
15. Cowin, S.C., Mehrabadi, M.M.: On the identification of material symmetry for anisotropic elastic materials. Q. J. Mech. Appl. Math. **40**, 451–476 (1987). https://doi.org/10.1093/qjmam/40.4.451
16. Mehrabadi, M.M., Cowin, S.C.: Eigentensors of linear anisotropic elastic materials. Q. J. Mech. Appl. Math. **43**, 15–41 (1990). https://doi.org/10.1093/qjmam/43.1.15
17. Böhlke, T., Jöchen, K., Kraft, O., Löhne, D., Schulze, V.: Elastic properties of polycrystalline microcomponents. Mech. Mater. **42**, 11–23 (2010). https://doi.org/10.1016/j.mechmat.2009.08.007
18. Böhlke, T., Lobos, M.: Representation of Hashin–Shtrikman bounds of cubic crystal aggregates in terms of texture coefficients with application in materials design. Acta Mater. **67**, 324–334 (2014). https://doi.org/10.1016/j.actamat.2013.11.003
19. Baerheim, R.: Harmonic decomposition of the anisotropic elasticity tensor. Q. J. Mech. Appl. Math. **46**, 391–418 (1993). https://doi.org/10.1093/qjmam/46.3.391
20. Haldipur, P., Margetan, F., Thompson, R.: Estimation of single-crystal elastic constants from ultrasonic measurements on polycrystalline specimens. AIP Conf. Proc. **700**, 1061–1068 (2004). https://doi.org/10.1063/1.1711735
21. Martin, G., Ochoa, N., Saï, K., Hervé-Luanco, E., Cailletaud, G.: A multiscale model for the elastoviscoplastic behavior of directionally solidified alloys: application to FE structural computations. Int. J. Solids Struct. **51**, 1175–1187 (2014). https://doi.org/10.1016/j.ijsolstr.2013.12.013
22. Jothi, S., Merzlikin, S.V., Croft, T.N., Andersson, J., Brown, S.G.R.: An investigation of micro-mechanisms in hydrogen induced cracking in nickel-based superalloy 718. J. Alloy. Compd. **664**, 664–681 (2016). https://doi.org/10.1016/j.jallcom.2016.01.033
23. Kobylinski, J.V., Lawitzki, R., Hofmann, M., Krempaszky, C., Werner, E.: Micromechanical behavior of Ni-based superalloys close to the yield point: A comparative study between neutron diffraction on different polycrystalline microstructures and crystal plasticity finite element modelling. Continuum Mech. Therm. **31**, 691–702 (2019). https://doi.org/10.1007/s00161-018-0720-0
24. Böhlke, T., Bertram, A.: Isotropic orientation distributions of cubic crystals. J. Mech. Phys. Solids **49**, 2459–2470 (2001). https://doi.org/10.1016/S0022-5096(01)00063-1
25. Stahn, O., Müller, W.H., Bertram, A.: Distances of Stiffnesses to Symmetry Classes. J. Elast. **141**, 349–361 (2020). https://doi.org/10.1007/s10659-020-09787-4
26. Francois, M., Geymonat, G., Berthaud, Y.: Determination of the symmetries of an experimentally determined stiffness tensor: Application to acoustic measurements. Int. J. Solids Struct. **35**, 4091–4106 (1998). https://doi.org/10.1016/S0020-7683(97)00303-X